Supplementary Materials for

Analysis of the liquid column atomization by the annular dual-nozzle gas jet flow

Daehyun Choi[1], Jungwon Byun[2] & Hyungmin Park[1,3,*]

[1]Department of Mechanical Engineering, Seoul National University, Seoul 08826, Korea

[2]Global Technology Center, Samsung Electronics, Suwon 16677, Korea

[3]Institute of Advanced Machines and Design, Seoul National University, Seoul 08826, Korea

List of movies

Movie S1. The disintegration process of the falling water column by the gas jet depending on the momentum flux ratio (m_{12}): (a) m_{12} = 0, (b) 0.17, (c) 0.27 (We_{eff2} = 28 – 252, Re_2 = 1.1 × 10^5) (d) 0.27 (We_{eff2} = 52 – 468, Re_2 = 1.5 × 10^5). For all cases, θ_2 = 40˚ and m_{L2} = 0.051, except (d) which is m_{L2} = 0.027.

Movie S2. The atomization process of the falling water column depending on the momentum flux ratio of the liquid to the lower gas jet: (a, b) m_{L2} = 0.0056; (c) 0.051; (d) 0.14. For all cases, We_{eff2} = 112, Re_2 = 1.1 × 10^5, and θ_2 = 40˚.

Movie S3. The pre-atomized water column depending on the flux of upper jet (u_2 = 0): (a) M_{L1} = 0.2; (b) 0.12; (c) 0.095; (d) 0.078; (e) 0.067. Here, We_{eff1} = 4.6 – 13.8 and Re_1 = 4.9 - 8.5 × 10^4.

List of figures

Figure S1. The profile of (a) mean vertical velocity ($\bar{u}_y/u_2$) and (b) the horizontal r.m.s. velocity fluctuation ($u'_{x,rms}/u_2$) at y/D_2 = 0.25 - 1.00. The solid lines and symbol, respectively, correspond to the case of m_{L2} = 0 and 0.009, without and with the liquid column, respectively. For all cases, m_{12} = 0.27, θ_2 = 20°, We_{eff1} = 13.6, We_{eff2} = 52.0.

Figure S2. Estimation on the jet exit velocity of (a) the upper nozzle and (b) the lower velocity, depending on the vertical location (y/D_2): For (a), ●, applied pressure p_1 = 0.2 MPa; ▲, 0.4 MPa and for (b), ▲, applied pressure p_2 = 0.025 MPa; ▼, 0.05 MPa; ●, 0.075 MPa; ■, 0.1 MPa. The open symbols correspond to the value measured by particle tracking velocimetry.

Figure S3. Relation between the applied pressure and the jet exit velocity of the lower (a) and the lower jet (b).

Figure S4. Schematic of the experimental setup for (a) the visualization of atomization process and (b) the measurement of droplet diameter.

Figure S5. Image processing to detect in-focused droplets obtained at the highest Weber number case of We_{eff1} = 13.8 and We_{eff2} = 468.0, respectively, while θ_2 = 40° and m_{L2} = 0.027: (a) raw droplet image, (b) binarization using adaptive threshold technique, (c) filling-the-hole technique and (d) selection of the in-focused droplet. In (d), the valid droplets are filled with yellow color, and the excluded droplets are filled with gray color.

Figure S6. The probability density function (PDF) of the droplet size for the case of (a) m_{L2} = 0.051, We_{eff2} = 112 and (b) m_{L2} = 0.027, We_{eff2} = 208: ●, N = 100; ▲, 500; ■, 1000. ◆, 10000 (where N denotes the total number of droplets). For all cases, m_{12} = 0 and θ_2 = 40°.

Figure S7. The convergence test for Sauter-mean-diameter of atomized droplet for θ_2 = 20°: ○, We_{eff1} = 4.6, We_{eff2} = 28.0; ■, We_{eff1} = 7.3, We_{eff2} = 52.0; ▲, We_{eff1} = 8.9, We_{eff2} = 28.0; ●, We_{eff1} = 13.6, We_{eff2} = 52.0.

Figure S8. (a) The representative shadow image of the oscillating liquid column with its center drawn as a dashed line and (b) the magnitude contour of the frequency at each vertical location calculated using the fast Fourier transform.

Figure S9. The dominant frequency depending on (a) the nozzle angle (θ_2) and (b) the flow regime: open symbol, m_{L2} = 0.051, We_{eff2} = 28 - 252; close symbol, m_{L2} = 0.027, We_{eff2} = 52 - 268. In (a), ○, m_{12} = 0; ▽, 0.11; □, 0.17; ◇, 0.27.

Figure S10. Control volume analysis to consider the interfacial friction owing to the presence of liquid lump. Here, S_i denotes the interfacial surface between the liquid lump and gas flow.

Figure S11. The length ratio (d_{32}/λ_{KH}) depending on the Weber number for the droplet atomization regime (□). The circle symbols (○: Rayleigh-Taylor (RT) regime and ●: Kelvin-Helmholtz (KH) regime) are from Sharma *et al*. (2021).

Comparison of single-phase and two-phase gas velocities

Because of the presence of atomized droplets and liquid interface, it is expected that the gas velocity measurement will be affected by the shadows, strong light reflection from the interface and the relatively lower speed of droplet in the same image. Thus, it was not allowed to validate the gas velocity measurement at the regions where these influences are substantial. Thus, we evaluated the two-phase velocity fields outside of the liquid column (at $x/D_2 > 0.2$) for $m_{L2} = 0.009$. Figure S1 shows the profile of mean vertical velocity and r.m.s. horizontal velocity fluctuation along the streamwise location for $m_{L2} = 0$ (without the liquid column) and 0.009 (with the liquid column). The operational conditions are $m_{12} = 0.27$, $\theta_2 = 20°$, $We_{eff1} = 13.6$, and $We_{eff2} = 52.0$. It is clear that the mean and fluctuating gas velocities are not affected significantly by the presence of the liquid column. At the downstream locations at $y/D_2 > 0.75$, the liquid phase tends to decelerate the gas flow and increase the turbulence of the gas-phase flow slightly, but the primary atomization of the present configuration occurs at $y/D_2 < 0.5$, as explained. Based on this comparison, it is understood that the statistics of gas-phase outside of the liquid flow would not change significantly, despite the widespread of the spray along the horizontal direction.

Estimation on the jet exit velocity

Due to the inherent limitation of PIV, the area near the jet exit could not be measured with PIV (section 2.2). However, the jet exit velocity is necessary to calculate *Re*, *We* and momentum ratio to define the characteristics of the jet. Here, the exit velocity of the jet is estimated using the particle tracking velocimetry and the conservation of momentum at the jet exit. From the equation (4.2) and using the control volume C_2 in figure 14, the following relationship can be deduced when $u_2 = 0$:

$$\widehat{v_{4G}}^2 A_4 = u_1^2 A_1. \tag{S1}$$

From this equation, the exit velocity of upper nozzle (u_1) can be theoretically calculated as:

$$u_1 = \left(\widehat{v_{4G}}^2 A_4/A_1\right)^{1/2} = \left(\int_{S_3} v_{3i}(v_{3i}\cdot\bar{n})dA \cdot A_4/A_1\right)^{1/2}. \tag{S2}$$

Likewise, the exit speed of the upper nozzle (u_2) can be calculated, substituting $u_1 = 0$:

$$u_2 = \left(\widehat{v_{4G}}^2 A_4/A_1\right)^{1/2} = \left(\int_{S_3} v_{3i}(v_{3i}\cdot\bar{n})dA \cdot A_4/A_1\right)^{1/2}. \quad \text{(S3)}$$

Note that the exit velocity u_1 and u_2 are the function of vertical location (y) of S_3. The experiment data are applied to the equations (S2) and (S3). And the result for the upper and the lower jet is shown in figures S2(a) and (b), respectively. For all velocities, it becomes constant after y/D = 0.6, and gradually decreases after that. Here, we infer the jet exit velocity by averaging the values for y/D = 0.6-1.0. On the other hand, the value obtained by using particle tracking velocimetry at the jet exit is displayed on the y-axis in open symbols. In order to predict the jet outlet velocity under various pressure conditions, the jet outlet velocities versus applied pressure are plotted (figure S3). Here, it was experimentally found that the jet outlet velocity is proportional to the third power of the applied pressure. Through this, the following was obtained.

$$u_{1,2} = c \cdot p_{1,2}^{1/3}. \quad \text{(S4)}$$

The proportional constant (c) for the upper nozzle and the lower nozzle could be 240 and 145, respectively. Through this equation, the jet exit velocity under various experimental conditions was inferred and the main dimensionless number (*Re*, *We*, momentum flux ratio) was calculated.

PDF of the atomized droplet size

Figure S6 shows representative PDF distribution of the droplet size. To obtain statistically valid data for droplet diameter, the total number of droplets should be sufficient. As seen in the figure, the distribution of droplet size becomes converged after N > 500, while the number of detected droplets is larger than 10,000. Thus, we thought that the PDF is converged and the averaged droplet size is appropriate for further analysis. In addition, the PDF distribution follows the gamma distribution due to the size polydispersity of liquid breakup as discussed by Villermaux *et al*. (2004) and Bremond *et al*. (2007).

Convergence of the measured droplet size

First, we estimated the characteristic time scale for the liquid breakup using the Rayleigh-Taylor instability, which governs the disintegration process in this study. From the equation

(4.10) in the main manuscript, the maximum growth rate ($\omega_{i,max}$) determines the breakup time ($T_b = 2\pi/\omega_{i,max}$) and is calculated as below (Marmottant & Villermaux 2004).

$$\omega_{i,max} = \left(\frac{2}{3\sqrt{3}}\right)^{1/2} \left(\frac{\rho_l a^3}{\sigma}\right)^{1/4}.$$

Here, ρ_l, a, and σ is the liquid density, acceleration of interface, and the coefficient of surface tension, respectively. Using the interfacial acceleration estimated in equation (4.11), the growth rate is obtained as 15.2 - 1809.3 m/s^2, corresponding to $\omega_{i,max}$ of 52.3 - 1881.7 1/s. Thus, the breakup time-scale is estimated as T_b = 0.0033 - 0.12 sec. For the atomized droplet size measurements, we obtained 300 images at the speed of 200 Hz, which means the total measurement time (T_m) of 1.5 sec. In figure S7, we have plotted the variation of droplet size (d_{32}) with T_m/T_b, for selected cases. The cases were chosen for the higher possibility of not achieving the convergence. As shown, the droplet size seems to be converged statistically for the tested cases.

Flapping frequency of the liquid column

The successive images of high-resolution (500 × 1000 pixels) were used to measure the dominant frequencies using the fast Fourier transform. The capturing rate ranges as 1,710-10,300Hz, indicating that the maximum measurable frequency is 805-5,150Hz by the Nyquist sampling theorem. Knowing that the reported frequencies of the liquid column flapping in previous studies (Marmottant & Villermaux 2004), this measurement range is sufficient for extracting the most dominant frequency representing the present unsteadiness. To obtain the dominant frequencies, the images are binarized with the specific threshold so that the edge of the liquid phase is clearly distinguished from the background. At a given vertical location, the horizontal center of the liquid area is collected (the location is drawn in figure S8(a) as a dashed line) for all times, and the fast Fourier transform is applied to find the magnitude of each frequency at every vertical location (figure S8b).

Figure S9(a) shows the variation of the dominant frequency (f_d), depending on the lower nozzle angle (θ_2), for the operation conditions of m_{L2} = 0.027 - 0.051, We_{eff2} = 28 - 468, and m_{12} = 0 - 0.27. The measured frequency is in the same range of previous studies (Marmottant & Villermaux 2004; Tian *et al*. 2014). For the present data, it is observed that the most dominant

frequency decreases with increasing of θ_2. The low frequency (< 50 Hz) at $\theta_2 > 40°$ is attributed to the wake-like flow structure made by the lower jet with the steep angle while the fast oscillatory behavior for $\theta_2 = 20°$ is attributed to the resemblance to the coaxial flow. On the other hand, it is observed that m_{12} and f_d are weakly correlated, which is possibly because the upper jet becomes strong enough to alter the global flow from the wake-like to the coaxial-like flows.

To examine the relation between the flow regime and the frequency, the dominant frequency is plotted at each flow regime in figure S9(b). It is clear that the flow regime having the back-flow structure is characterized by the lower frequency (< 50Hz) since the wake-like behavior of gas-phase slows down the liquid oscillation. In contrast, if the upper jet overcomes the back flow and the flow regime becomes the bulk or droplet atomization regime, the flow structure has a high frequency (~ 100Hz) due to the coaxial-like behavior of the gas phase. The trend of frequency also provides quantitative evidence for flow regime classification between the back-flow and the non-backflow regimes.

Effect of liquid interface on the gas velocity: control volume analysis

To estimate the liquid-induced deviation in the mean gas velocity for all locations, we need the spatial distribution of velocity, size, and volume fraction of dispersed phase, with varying conditions, which is unfortunately not allowed in the present setup. However, our major interest is focused on the primary atomization site near the nozzle (usually $y/D_2 > -0.5$), and we tried to estimate the two-phase flow near the upper-nozzle section, $-0.5 < y/D_2 < 0.5$, where the upper jet and the liquid column interact. In figure S10, we have illustrated the control volume (C_3) to analyze this. Here, the upper gas jet is generally dragged by the lower-speed liquid flow and the gas velocity at the interface is the minimum. The interfacial velocity is modeled as $u_i = (\sqrt{\rho_L}u_L + \sqrt{\rho_G}u_1)/(\sqrt{\rho_L} + \sqrt{\rho_G})$ assuming that the dynamic pressure balances through the transverse direction (Dimotakis 1986), and is calculated as $u_i/u_1 = 0.045$ - 0.055. The thickness of this low-speed region (relevant to the shear-layer thickness) is obtained as the vorticity length, $\delta_\omega = 0.17(1 - r)/(1 + r) \cdot l_m$, where $r = u_1/u_L$ and l_m denotes the streamwise length of the mixing layer. δ_ω/D_2 is calculated as 0.081 - 0.083 at the lower nozzle exit ($y = 0$). We assumed that the shear layer evolves linearly from the liquid surface expanding horizontally about half the thickness of the vorticity layer ($\delta_\omega/2$). Thus, the net gas velocity ($\hat{v}'_{3G}$)

decelerated by the interaction with the liquid column can be calculated by modifying the equation (4.3) in the main text, as follows.

$$\rho_G \hat{v}'_{3G} |\hat{v}'_{3G}| A_{3G} = \int_{S_3} p_{3G} dA - \rho_G v_1^2 A_1 - \int_{S_4} \tau_s dA. \quad \text{(S5)}$$

Here, S_4 denotes the interface between gas and liquid with the velocity of u_i, and the frictional stress (τ_s) there can be expressed as $\tau_s \simeq \mu(u_1 - u_i)/\delta_\omega$, where μ is the kinematic viscosity of the gas. Using the representative value of $u_i/u_1 = 0.05$ and $0.5\delta_\omega/D_2 = 0.04$, the contribution by the viscous stress is calculated as $\int_{S_i} \tau_s dA \simeq \mu(u_1 - u_i)/\delta_\omega \cdot \pi D_L h_2$. Compared to the single-phase gas flow contributed by the momentum of the upper jet, it is estimated that the deceleration of $\hat{v}'_{3G}$ is approximately 1.68% (below 2%), supporting our original assumption, i.e., the analysis with the single-phase (gas velocity) only is reasonable.

Examination on the transition of breakup mechanism

We examined whether the transition from the Rayleigh-Taylor (RT) to the shear-induced Kelvin-Helmholtz (KH) instability occurs in the present cases. According to Theofanous (2011), this transition starts at $We_d \sim 10^2$ (d, drop diameter) and completes at $We_d \gtrsim 10^3$ (at low $Oh < 0.1$). Oh is the Ohnesorge number. At this transition regime, the ratio between the droplet size and the instability length scale, i.e., d/λ_{KH}, determines the RT-to-KH transition, and its critical value is ~10 (Sharma *et al*. 2021). The regime map for RT and KH instability is shown in figure S11, reproduced from Sharma *et al*. (2021). For the droplet atomization regime, the droplet pre-atomized from the upper jet experiences another breakup with the lower nozzle. Looking closely, the droplets are affected by the high-speed freestream and the shear layer with the diffusion length occurs on its surface at the windward side. Using the dispersion relation (Marmottant & Villermaux 2004; Kim *et al*. 2006; Sharma *et al* 2021), the length scale of shear-induced instability (λ_{KH}) is obtained as $\lambda_{KH} = 2\pi/1.5 \cdot \delta_a \sqrt{\rho_l/\rho_g}$ where $\rho_{l,g}$ denote the density of liquid and gas, respectively. Here, δ_a is the boundary-layer thickness of the air phase and can be determined using boundary-layer analysis (Kim *et al*. 2006; Jalaal & Mahravaran 2014) as $\delta_a = K \cdot l_c/Re_{l_c}$ where l_c corresponds to the characteristic length and is set to $d/2$ (Sharma *et al*. 2021). The Reynolds number (Re_{l_c}) is defined as $\rho_g u_i l_c/\mu_g$. The scaling constant (K) is set to 0.12 given from the experiment and simulation of droplet differentiation

(Kim *et al*. 2006; Jalaal & Mahravaran 2014; Sharma *et al*. 2021), and the effective gas velocity (u_{eff}) is used as a characteristic velocity (u_i) like the estimation of We_{eff} (see §2.4). The Weber number (We_d) can be calculated as $We_d = \rho_g u_{eff}^2 d/\sigma$ (σ: the surface tension). Here, we used the droplet size (d) when the lower nozzle is absent (figure 20) since the fragmentation process of the liquid column at the upper gas jet ($y > 0$) is less perturbed by the lower gas jet. Among the cases in the regime map (figure 13), three conditions ($m_{12} = 0.27$ and $\sin\theta_2 = 0.34 – 0.64$) belong to the droplet atomization regime, and their length ratios and Weber numbers were plotted onto the figure S11. The figure shows that our cases mainly lie on the RT regime, while the case of the highest We (= 115) is on the border of the transition regime. The Low We ($\lesssim$ 100) indicates the low dynamics pressure which inhibits the KH instability to grow and gives sufficient time for slowly-growing RT instability (Theofanous 2011; Theofanous *et al*. 2012). Additionally, the length ratios are below the threshold ($d/\lambda_{KH} = 10$). Since the shear-induced instability only develops at the sufficiently high wavenumber (i.e., high d/λ_{KH}), the λ_{KH} comparable to the droplet diameter ($\sim 1.23d$) in the present study also obstructs the growth of the KH instability. It should be noted that, if the We_d increases further than our range (e.g., by increasing applied pressure in Table 1), the KH instability should be eventually triggered, as expected from figure S11.

References

Bremond, N., Clanet, C. & Villermaux, E. 2007 Atomization of undulating liquid sheets. *J. Fluid. Mech.,* **585**, 421-456.

Dimotakis, P. E. 1986 Two-dimensional shear-layer entrainment. *AIAA J*., **24**, 1791-1796.

Jalaal, M., & Mehravaran, K. 2014 Transient growth of droplet instabilities in a stream. *Phys. Fluids* **26**, 012101.

Kim, D., Desjardins, O., Herrmann, M., & Moin, P. 2006 Toward two-phase simulation of the primary breakup of a round liquid jet by a coaxial flow of gas. In *Center for Turbulence Research, Annual Research Briefs*, pp.185-195. Stanford University.

Marmottant, P. & Villermaux, E. 2004 On spray formation. *J. Fluid Mech*., **498**, 73-111.

Sharma, S., Singh, A. P., Rao, S. S., Kumar, A., & Basu, S. 2021 Shock induced aerobreakup of a droplet. *J. Fluid. Mech.* **929**, A27.

Theofanous, T. G. 2011 Aerobreakup of Newtonian and viscoelastic liquids. *Annu. Rev. Fluid Mech.* **43**, 661-690.

Theofanous, T. G., Mitkin, V. V., Ng, C. L., Chang, C. H., Deng, X., & Sushchikh, S. 2012 The physics of aerobreakup. II. Viscous liquids. *Phys. Fluids* **24**, 022104.

Tian, X. S., Zhao, H., Liu, H. F., Li, W. F., & Xu, J. L. 2014 Effect of central tube thickness on wave frequency of coaxial liquid jet. *Fuel Process. Technol.*, **119**, 190-197.

Villermaux, E., Marmottant, P., & Duplat, J. 2004 Ligament-mediated spray formation. *Phys. Rev. Lett.*, **92**, 074501.

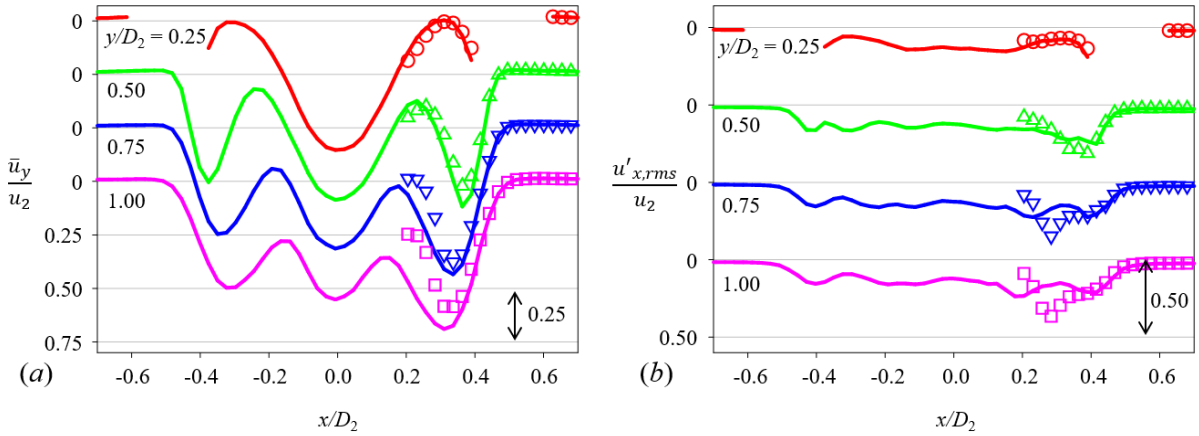

Figure S1. The profile of (a) mean vertical velocity ($\bar{u}_y/u_2$) and (b) the horizontal r.m.s. velocity fluctuation ($u'_{x,rms}/u_2$) at y/D_2 = 0.25 - 1.00. The solid lines and symbol, respectively, correspond to the case of m_{L2} = 0 and 0.009, without and with the liquid column, respectively. For all cases, m_{12} = 0.27, θ_2 = 20°, We_{eff1} = 13.6, We_{eff2} = 52.0.

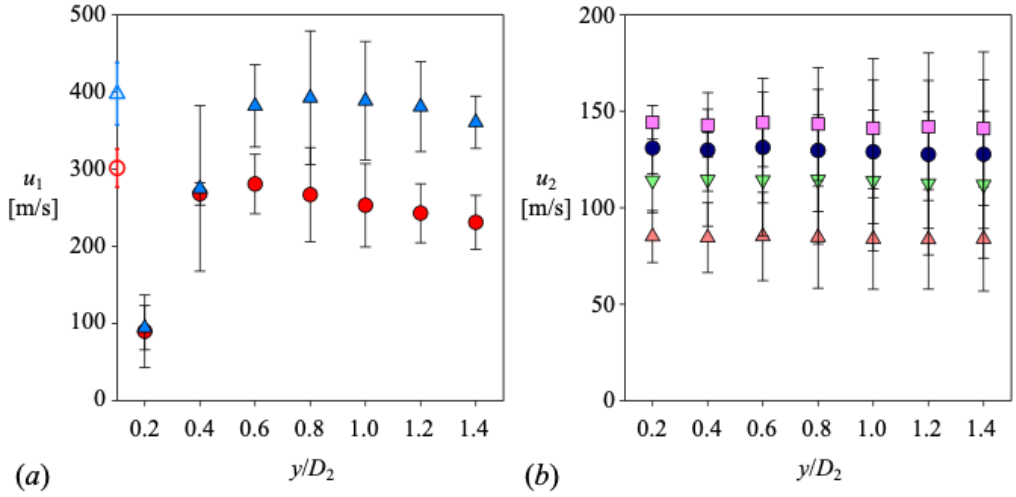

Figure S2. Estimation on the jet exit velocity of (a) the upper nozzle and (b) the lower velocity, depending on the vertical location (y/D_2): For (a), ●, applied pressure p_1 = 0.2 Mpa; ▲, 0.4 Mpa and for (b), ▲, applied pressure p_2=0.025Mpa; ▼, 0.05Mpa; ●, 0.075Mpa; ■, 0.1Mpa. The open symbols correspond to the value measured by particle tracking velocimetry.

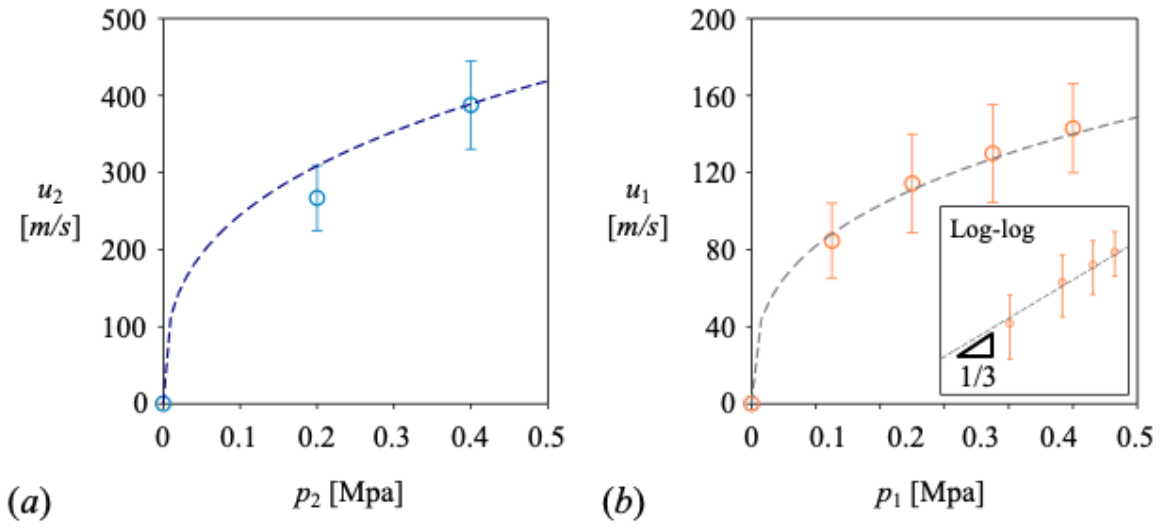

Figure S3. Relation between the applied pressure and the jet exit velocity of the lower (a) and the lower jet (b).

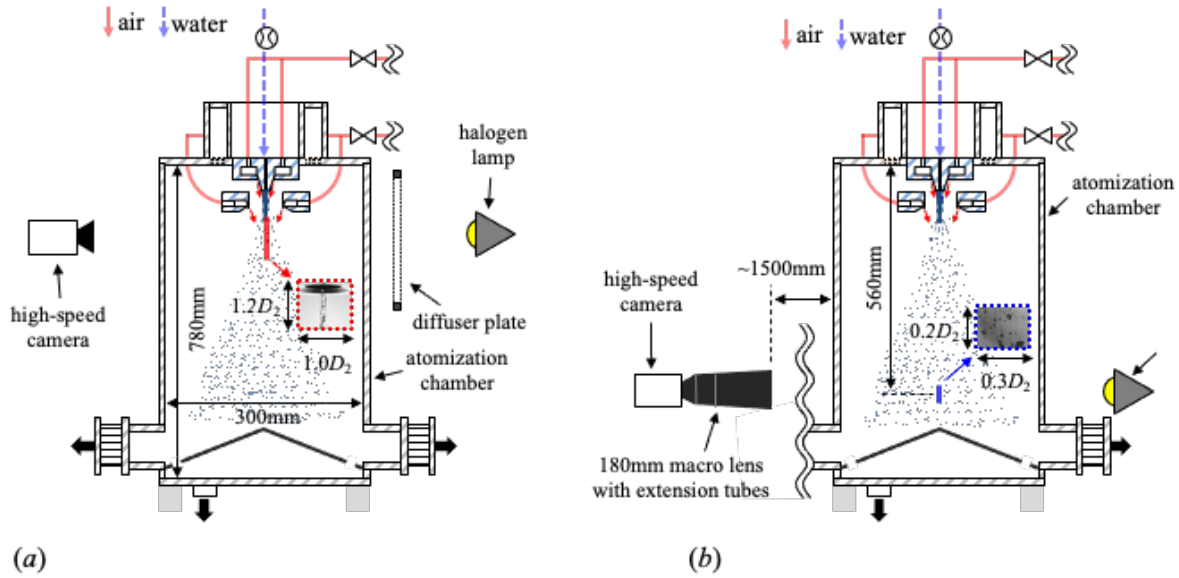

Figure S4. Schematic of the experimental setup for (a) the visualization of atomization process and (b) the measurement of droplet diameter.

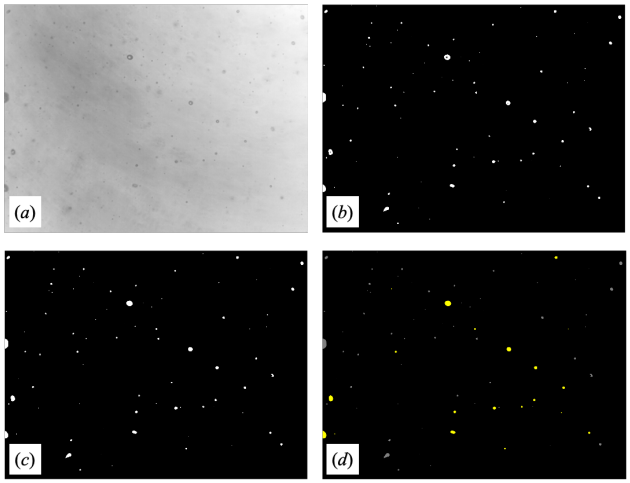

Figure S5. Image processing to detect in-focused droplets obtained at the highest Weber number case of $We_1 = 1.7 \times 10^3$ and $We_2 = 5.2 \times 10^3$, which corresponds to $We_{\mathrm{eff},1} = 14.4$ and $We_{\mathrm{eff},2} = 253.0$, respectively, while $\theta_2 = 40^\circ$ and $m_{L2} = 0.027$: (a) raw droplet image, (b) binarization using adaptive threshold technique, (c) filling-the-hole technique and (d) selection of the in-focused droplet. In (d), the valid droplets are filled with yellow color, and the excluded droplets are filled with gray color.

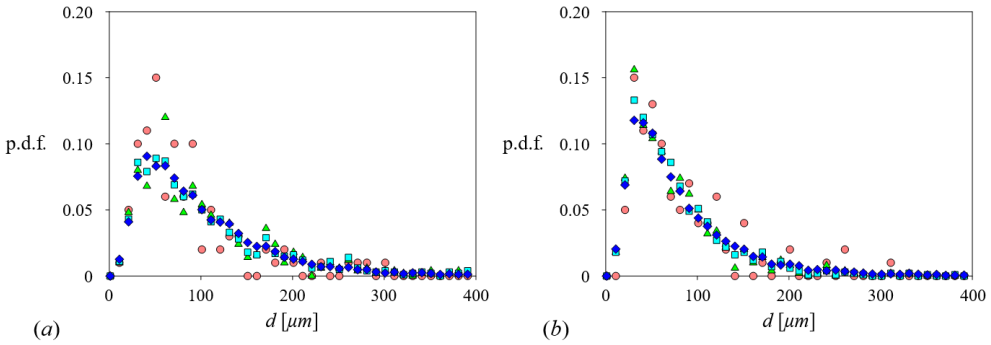

Figure S6. The probability density function (PDF) of the droplet size for the case of (a) $m_{L2} = 0.051$, $We_{eff2} = 112$ and (b) $m_{L2} = 0.027$, $We_{eff2} = 208$: ●, $N = 100$; ▲, 500; ■, 1000. ◆, 10000 (where N denotes the total number of droplets). For all cases, $m_{12} = 0$ and $\theta_2 = 40°$.

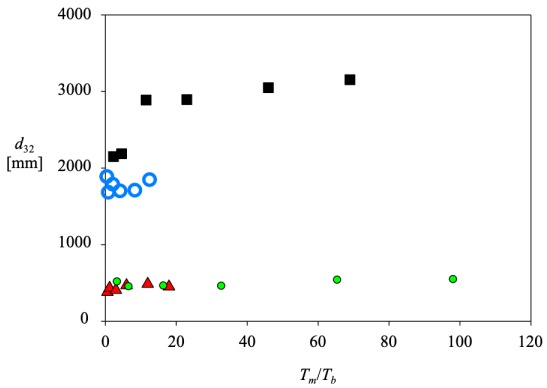

Figure S7. The convergence test for Sauter-mean-diameter of atomized droplet for $\theta_2 = 20°$: ○, $We_{eff1} = 4.6$, $We_{eff2} = 28.0$; ■, $We_{eff1} = 7.3$, $We_{eff2} = 52.0$; ▲, $We_{eff1} = 8.9$, $We_{eff2} = 28.0$; ●, $We_{eff1} = 13.6$, $We_{eff2} = 52.0$.

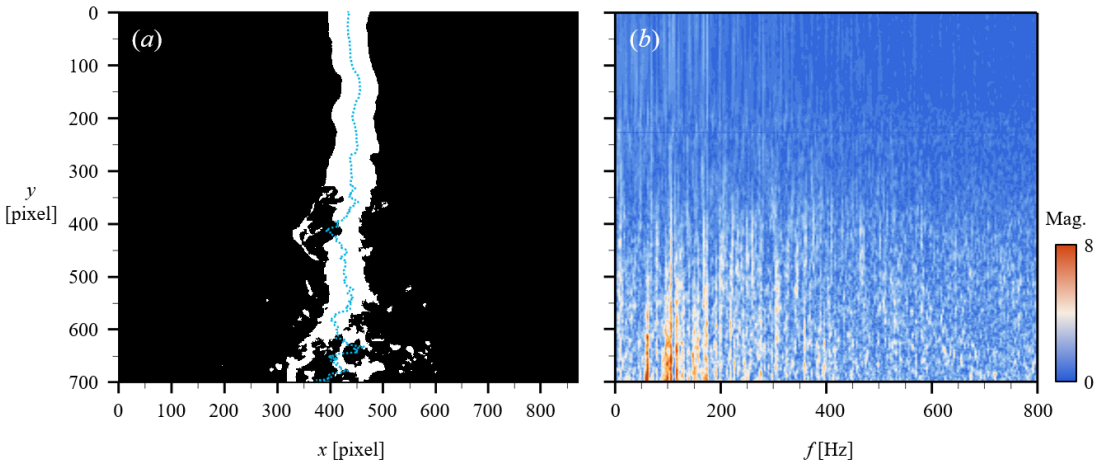

Figure S8. (a) The representative shadow image of the oscillating liquid column with its center drawn as a dashed line and (b) the magnitude contour of the frequency at each vertical location calculated using the fast Fourier transform.

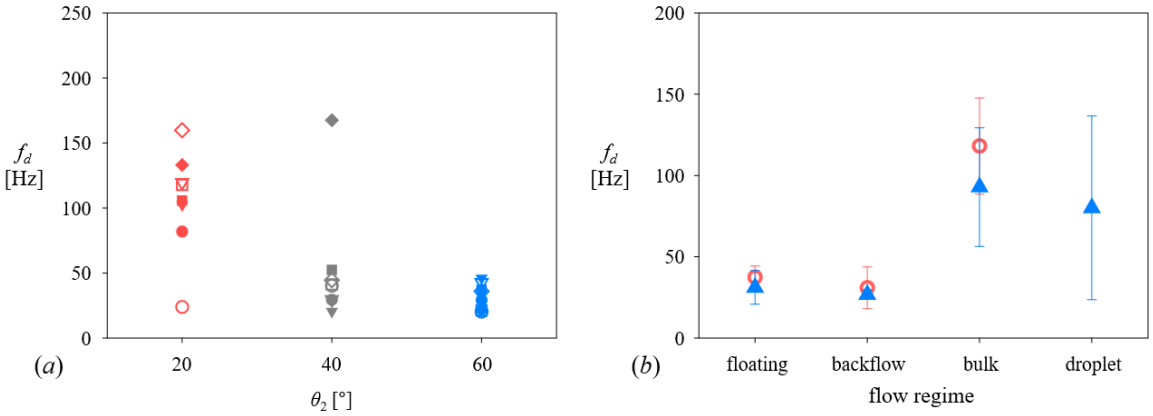

Figure S9. The dominant frequency depending on (a) the nozzle angle (θ_2) and (b) the flow regime: open symbol, m_{L2} = 0.051, We_{eff2} = 28 - 252; close symbol, m_{L2} = 0.027, We_{eff2} = 52 - 468. In (a), ○, m_{12} = 0; ▽, 0.11; □, 0.17; ◇, 0.27.

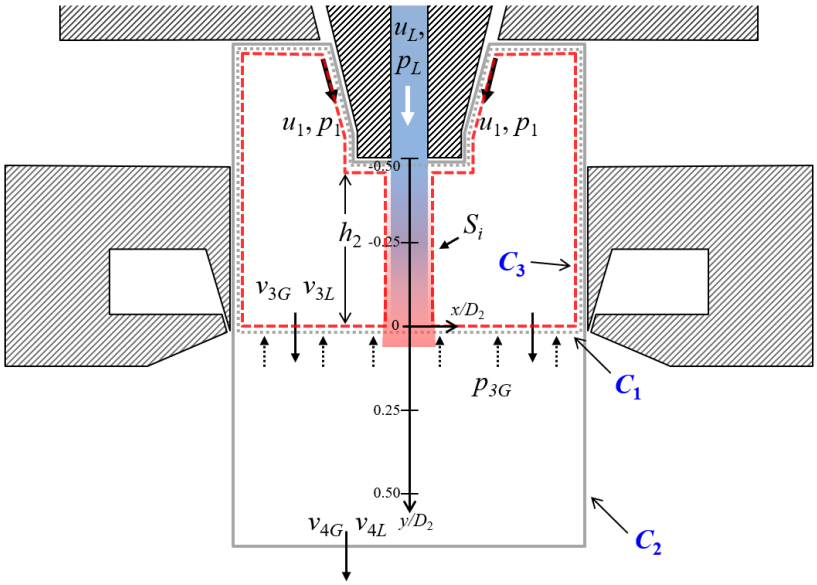

Figure S10. Control volume analysis to consider the interfacial friction owing to the presence of liquid lump. Here, S_i denotes the interfacial surface between the liquid lump and gas flow.

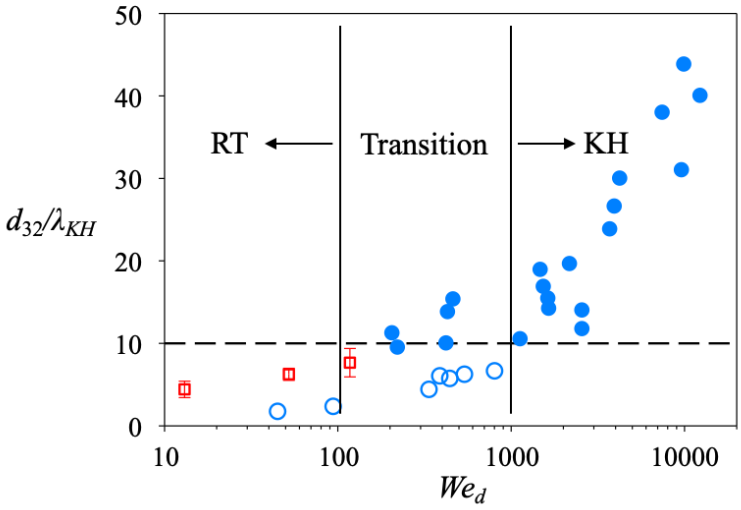

Figure S11. The length ratio (d_{32}/λ_{KH}) depending on the Weber number for the droplet atomization regime (□). The circle symbols (○: Rayleigh-Taylor (RT) regime and ●: Kelvin-Helmholtz (KH) regime) are from Sharma *et al.* (2021).